

Electronic properties of structural twin and antiphase boundaries in materials with strong electron-lattice couplings

K. H. Ahn*, T. Lookman, A. Saxena, and A. R. Bishop

Theoretical Division, Los Alamos National Laboratory, Los Alamos, New Mexico 87545

Using a symmetry-based atomic scale theory of lattice distortions, we demonstrate that elastic textures, such as twin and antiphase boundaries, can generate intricate electronic inhomogeneities in materials with strong electron-lattice coupling, as observed in perovskite manganites and other functional materials.

PACS numbers: 73.20.-r, 75.47.Gk, 68.35.-p, 74.81.-g

Recent advances in imaging techniques have revealed the presence of rich elastic textures in functional materials such as colossal magnetoresistive (CMR) manganites,^{1,2} ferroelectrics,³ ferroelastics,⁴ and shape memory alloys.⁵ In particular, recent experiments on certain perovskite manganites compounds² have shown the correlation between electronic transport properties and the presence of meandering antiphase boundaries (APBs) within insulating charge ordered domains, interpreted as the existence of metallic regions forming around APBs. It is also reported that strains near grain boundaries in thin film can modify electronic properties in manganites.⁶ The interplay between elastic texture and electronic heterogeneity is thus central to understanding multiphase coexistence and the resultant electronic properties in CMR and other functional materials.

In this Report, we illustrate the importance of elastic inhomogeneities in modifying electronic properties in materials with strong electron-lattice coupling. In particular, we study the electronic properties of APBs and twin boundaries (TBs) on a two-dimensional (2D) lattice. We first show how a recently-developed symmetry-based atomic-scale theory of lattice distortions can be used to find atomic configurations of twin and antiphase boundaries. Within our framework, we illustrate the differences and similarities between TBs and APBs from the point of view of localization of long [short] wavelength modes inside APBs [TBs], evolution upon energy relaxation and roughness⁷ [smoothness] of APBs [TBs]. We subsequently perform a tight binding calculation with a Su-Schrieffer-Heeger (SSH) type model of electron-lattice coupling to predict the distribution of electronic density of states, which can be related to the results of scanning tunneling microscope (STM) measurements. Our work thus forms the basis for predicting electronic properties from pre-designed materials microstructures.

Twin boundaries separate domains related by the rotation of crystalline axes, whereas APBs represent boundaries at which the sequence of alternating distortions, such as alternating rotational directions of oxygen octahedra in perovskite oxides, change their phase (i.e., broken translational symmetry). Although our method can be applied to 2D or 3D lattices with mono- or multiatomic bases, we illustrate our ideas with a square lattice in 2D space with a monatomic basis, for which

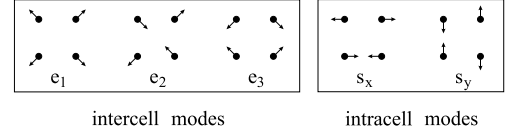


FIG. 1: Distortion modes for a square lattice in 2D with a monatomic basis.⁸ For example, $s_x(\vec{i}) = [d^x(\vec{i}) - d^x(\vec{i} + (10)) + d^x(\vec{i} + (11)) - d^x(\vec{i} + (01))]/2$, where $d^x(\vec{i})$ and $d^y(\vec{i})$ represent the displacement of the atom at site \vec{i} along x and y directions respectively.

the appropriate atomic scale distortion variables are the modes shown in Fig. 1 (Ref. 8). These modes have important advantages over displacement variables – they reflect the symmetries of the lattice and can serve as order parameters (OP) in structural phase transitions. Therefore, energy expressions with desired ground states can be written in a simpler way in these variables than in usual displacement variables. Moreover, since the lattice distortions are decomposed into the modes at $\vec{k} = (0, 0)$ (long-wavelength or intercell modes) and $\vec{k} = (\pi, \pi)$ (short-wavelength or intracell modes), the approach using these modes shows the differences between long and short wavelength lattice distortions in a natural way.

We consider APBs, such as the one shown in Fig. 2 where open circles represent the distorted atomic positions, for s_x or s_y modes. The simplest energy expression yielding a ground state with either pure s_x or s_y mode lattice distortion is

$$E_{\text{ssxy}} = \sum_{\vec{i}} -\frac{D}{2} [s_x(\vec{i})^2 + s_y(\vec{i})^2] + \frac{G_1}{4} [s_x(\vec{i})^4 + s_y(\vec{i})^4] + \frac{G_2}{2} s_x(\vec{i})^2 s_y(\vec{i})^2 + \sum_{\vec{i}, n=1,2,3} \frac{C_n}{2} e_n(\vec{i})^2, \quad (1)$$

where the coefficients D , G_1 , G_2 (with $G_1 < G_2$) can be obtained from interatomic forces and C_n are the associated elastic moduli.

Since the ground state has $\vec{k} = (\pi, \pi)$ component lattice distortions, we define variables with tilde by multiplying $(-1)^{i_x+i_y}$ with all intercell/intracell/displacement variables [e.g., $\tilde{s}_x(\vec{i}) = s_x(\vec{i})(-1)^{i_x+i_y}$, $\tilde{d}_x(\vec{i}) = d_x(\vec{i})(-1)^{i_x+i_y}$]. In wavevector space, this corresponds to interchanging the

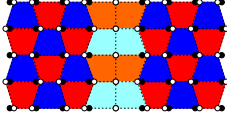


FIG. 2: (Color) An example of the atomic displacement pattern on either side of an APB. Solid and open circles represent the atomic positions for undistorted square lattice and distorted lattice, respectively. Red and blue represent the positive and negative signs of the s_x mode defined for each plaquette.

$(0,0)$ and (π,π) points. Therefore, \tilde{s}_x and \tilde{s}_y are the modes near $\vec{q} = (0,0)$, and \tilde{e}_1 , \tilde{e}_2 , and \tilde{e}_3 are the modes near $\vec{q} = (\pi,\pi)$, where \vec{q} represents the wavevector for the variables with tilde. The constraint equations⁸ in the continuum limit are $\tilde{e}_{1,3}(\vec{r}) = (\nabla_y \tilde{s}_x \pm \nabla_x \tilde{s}_y)/(2\sqrt{2})$ and $\tilde{e}_2(\vec{r}) = (\nabla_x \tilde{s}_x + \nabla_y \tilde{s}_y)/(2\sqrt{2})$. These relations show that spatial variations of *intracell* modes (\tilde{s}_x , \tilde{s}_y) always generate *intercell* modes (\tilde{e}_1 , \tilde{e}_2 , \tilde{e}_3), which becomes microscopic origin of the phenomenological gradient energy term in continuum elasticity theory. Therefore, intercell modes are present inside an APB at which an intracell mode with tilde changes its sign. Similar arguments apply to a TB⁸ – the spatial variations of intercell modes always generate intracell modes inside TB through their constraints – and lead to a similar solitary profile for TB and APB.^{4,9} However, there exists a fundamental difference between intercell and intracell modes: In the $k \rightarrow 0$ limit, e_1 , e_2 , and e_3 are given as a first derivative of d_x and d_y , whereas in the $q \rightarrow 0$ limit, \tilde{s}_x and \tilde{s}_y are $2\tilde{d}_x$ and $2\tilde{d}_y$. Therefore, e_1 , e_2 , and e_3 are related by constraint equations, whereas \tilde{s}_x and \tilde{s}_y are not constrained by each other.

We consider the APB between the two ground states with $\tilde{s}_x(\vec{i}) = \pm\sqrt{D/G_1}$ (Fig. 2). On expanding Eq. (1) around the ground state and retaining leading order terms, we write the energy $E_{\text{APB}} = E_{\text{APB,OP}} + E_{\text{APB,NOP}}$, where

$$E_{\text{APB,NOP}} = \sum_{\vec{i}, n=1,2,3} \frac{C_n}{2} \tilde{e}_n(\vec{i})^2 + \sum_{\vec{i}} \frac{D'}{2} \tilde{s}_y(\vec{i})^2 \quad (2)$$

$$E_{\text{APB,OP}} = \sum_{\vec{i}} -\frac{D}{2} \tilde{s}_x(\vec{i})^2 + \frac{G_1}{4} \tilde{s}_x(\vec{i})^4, \quad (3)$$

and $D' = D(G_2/G_1 - 1)$. The energy E_{APB} has the identical form to that for a TB with e_3 as OP⁸ – a double-well potential for OP and harmonic potentials for non-OP. For both TB and APB problems, the non-OP energy terms mediate an anisotropic interaction between OPs through the constraints. The minimization of $E_{\text{APB,NOP}}$ using Lagrange multipliers leads to $E_{\text{APB,NOP}}^{\text{min}} = \sum_{\vec{q}} \frac{1}{2} \tilde{s}_x(-\vec{q}) \tilde{U}(\vec{q}) \tilde{s}_x(\vec{q})$, where $\tilde{U}(\vec{q})$ has a q^2 leading order term with an anisotropic coefficient $U_2(\theta_q) = [(C_1 + C_2 + C_3) + (C_2 - C_1 - C_3) \cos 2\theta_q]/16$. When transformed into real space, the q^2 leading order term gives rise to a short range R^{-4} interaction between

OP \tilde{s}_x , where R is the distance between two sites, unlike the long-range R^{-2} interaction between OP e_3 for the TB case.^{10,11} Such different range of interaction is consistent with well-known understanding⁷ of smoothness of TB and roughness of APB, which our simulation reproduces below.

The physical origin of the long-range interaction between *intercell* modes and short-range interaction between *intracell* modes lies in the difference in the symmetry operations relating the two domains separated by a TB or APB. For a TB, the sign change in OP corresponds to a change in orientation, which has no intrinsic length scale and thus gives rise to a long range interaction. For an APB, the sign change in OP signifies translation of the configuration by one atomic spacing, implying the presence of an intrinsic atomic length scale that is responsible for the fast decay of the interaction between OPs. These considerations apply to any 2D/3D lattice with mono- or multiatomic bases. We can also expect it to be valid for the rough and fluctuating stripes suggested in high- T_C cuprates, which are examples of magnetic APBs. Arguments similar to those in Ref. 12, related to the range of the interactions, explain the characteristic smoothness and roughness of TBs and APBs.

The full expression of the kernel $\tilde{U}(\vec{q})$ in $E_{\text{APB,NOP}}^{\text{min}}$ is given by

$$\begin{aligned} \tilde{U}(\vec{q}) = & \frac{C_1 + C_3}{2} T_y(\vec{q})^2 + \frac{C_2}{2} T_x(\vec{q})^2 \\ & - \frac{(C_1 + C_2 - C_3)^2 T_x(\vec{q})^2 T_y(\vec{q})^2}{4D' + 2(C_1 + C_3)T_x(\vec{q})^2 + 2C_2T_y(\vec{q})^2}, \end{aligned} \quad (4)$$

where $T_x(\vec{q}) = \tan(q_x/2)$ and $T_y(\vec{q}) = \tan(q_y/2)$. We choose similar parameter values for both APB and TB cases and use the Euler method¹⁰ to relax the lattice starting from random initial conditions to see difference in evolution between TB and APB. The results, e_3 for TB and \tilde{s}_x for APB, on a 64×64 lattice with periodic boundary conditions are shown in Figs. 3 and 4, respectively, where the main panels show real space distributions and insets the k or q -space distributions. Figures 3(a) and 4(a) correspond to early stages of the relaxation, which show the characteristics of the OP distribution at high temperature(T), whereas Figs. 3(b) and 4(b) reflect the OP distributions for late stages at low T . Even at the early stage, the presence of the long range correlation between intercell OP along 45° and 135° can be identified in the main panel in Fig. 3(a), reminiscent of tweed structures in martensitic materials.¹⁰ The k -space distribution plotted in the inset of Fig. 3(a) shows strong preference of $e_3(\vec{k})$ along 45° and 135° orientations. Such long-range correlation and anisotropy are absent for the phase of the intracell mode distortion, as shown in Fig. 4(a). The late stage of the relaxation depicted in Figs. 3(b) and 4(b) show characteristic smooth TBs⁵ and rough APBs². The TB is metastable and cannot be removed by further relaxation, unless large noise is applied. In contrast, the APB in Fig. 4(b), which is a ring due to the periodic boundary condition, shrinks and disappears upon

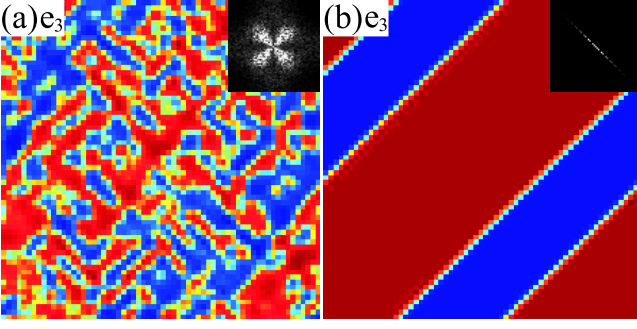


FIG. 3: (Color) $e_3(\vec{i})$ (main panels) and $|e_3(\vec{k})|$ (insets) obtained from simulation for TB: (a) early and (b) late stages of the lattice relaxation. Parameter values (see Ref. 8 for the definitions) are $A_1 = A_2 = B = 4$, $A_3 = 5$, and $F_3 = 50$. The center of the inset corresponds to $\vec{k} = 0$ and the four corners $\vec{k} = (\pm\pi, \pm\pi)$. (Dark red: 0.32, dark blue: -0.32, white color in the inset: larger than 0.2 times the maximum of $|e_3(\vec{k})|$).

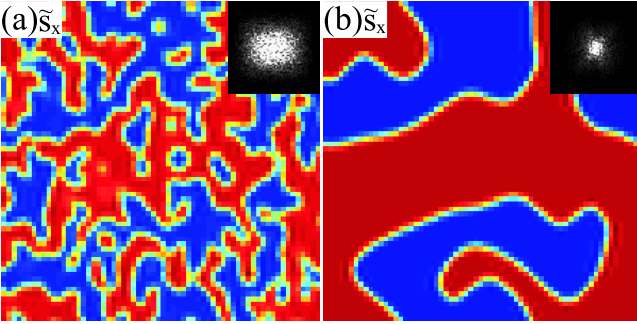


FIG. 4: (Color) $\tilde{s}_x(\vec{i})$ (main panels) and $|\tilde{s}_x(\vec{q})|$ (insets) distributions obtained from simulations for APB: (a) early and (b) late stage of the lattice relaxation. Parameter values are $C_1 = C_2 = C_3 = D' = 4$, $D = 5$, and $G_1 = 50$.

further relaxation. Although the solitary-wave profile of the smooth APB along a certain direction is a metastable state,⁴ the absence of a long range interaction between the phase of intracell mode distortions prevents the relaxation of random initial configuration from reaching such metastable states. This indicates that lattice defects or boundary conditions are necessary to reach the metastable solitary-wave APB configuration in materials, and influence the geometry of APBs.

To study functional electronic aspects associated with these TB and APB microstructures, we consider the modulation of electronic properties based on the following SSH electron-lattice coupling Hamiltonian,

$$H_{SSH} = \sum_{\vec{i}, a=x,y} -t_0[1 - \alpha(d_{i+\hat{a}}^2 - d_i^2)](c_i^\dagger c_{i+\hat{a}} + c_{i+\hat{a}}^\dagger c_i), \quad (5)$$

where c_i^\dagger is the creation operator for an electron at \vec{i} . We use $d^x(\vec{i})$ and $d^y(\vec{i})$ obtained from our atomistic model as inputs to the SSH Hamiltonian. For $t_0 = 1$, $\alpha = 1$, and the TB and APB results shown in Figs. 3(b) and 4(b), we find all energy levels and eigenstates numerically, and

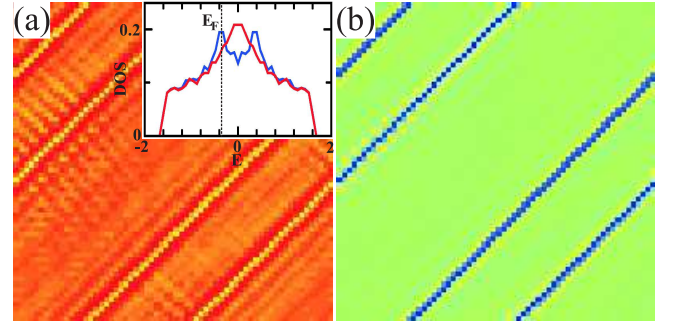


FIG. 5: (Color) Electronic properties calculated for the lattice distortion in Fig. 3(b). (a) Inset: local DOS within the domain (blue curve) and TB (red curve); main panel: spatial distribution of local DOS at E_F . (b) Corresponding charge density distribution (dark blue: 0.36, green: 0.39).

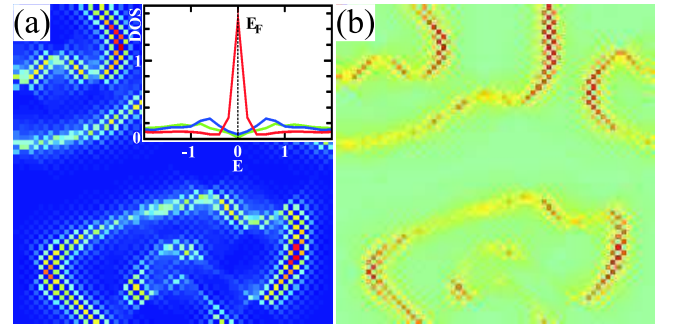


FIG. 6: (Color) Electronic properties calculated for the lattice distortion in Fig. 4(b). (a) Inset: local DOS within the domain (blue curve) and APB (red and green curves); main panel: spatial distribution of local DOS at $E_F = 0$ (dark blue: 0, dark red: 2). (b) Spatial charge density distribution for $E_F = 0.1$ (green: 0.52, dark red: 0.72).

calculate the local density of state (DOS) at each site and the distributions of local DOS and charge density for chosen Fermi energies (E_F), as shown in Figs. 5, 6 and 7.

The blue curve in the inset of Fig. 5(a) represents the local DOS within the domain of Fig. 3(b), close to the bulk DOS for the homogeneous phase. The energy difference between the two peaks is proportional to $\alpha|e_3|$. Within the TB, $|e_3|$ is small and therefore the local DOS spectral weight moves toward $E = 0$, as shown with a red curve. This local shift of the DOS weight can be measured using direct local probes, such as STM.^{1,13} For E_F shown in this inset, the local DOS is smaller inside the TB than inside the domain, and the main panel of Fig. 5(a) shows the real space distribution of local DOS at this E_F . The oscillation of local DOS within the domain is related to Friedel oscillations. The feedback from electron to lattice neglected here may generate a similar Friedel oscillation of the lattice. The charge density, which is the area in local DOS below E_F , is a constant (0.5) if $E_F = 0$. If $E_F < 0$, more electrons are depleted from the TB than the domain, as shown in Fig. 5(b).

The charge density also has a Friedel oscillation, though not clearly visible in Fig. 5(b).

The inset of Fig. 6(a) shows the local DOS for the APB case. Within the domain, each site has a neighbor along x axis that is closer in one direction and farther in the other (Fig. 2). Such a distortion pattern results in a V-shaped local DOS with zero DOS at $E = 0$, plotted as a blue curve in the inset of Fig. 6(a) (the small finite value of local DOS at $E = 0$ is due to the finite energy bin size). Within the APB, the average of the two bond lengths along x -axis has a (π, π) component. For example, along sites at the center of the 90° APB shown in Fig. 2, the neighboring sites in the x -direction are alternately closer or farther apart. The red line in the inset of Fig. 6(a) represents the local DOS for the sites with two farther neighbors within the center of APB. This has a peak near $E = 0$. The green line represents the local DOS at sites with two closer neighbors, right next along y direction to the sites for the red curve. The difference between the red and green curves emphasizes the difference that occurs in density of states due to atomic-scale changes in microstructure as along an APB. Such atomistically sharp changes at structural interfaces have been seen in CMR manganites with STM (Renner *et al.*¹). The local DOS at $E_F = 0$ is zero within the domain and finite only around the APB with a (π, π) component modulation, as depicted in the main panel of Fig. 6(a). This means that the electronic states created by the APB dominate the low energy properties of the whole system, e.g., conductivity or specific heat. The charge density for E_F slightly higher than zero is plotted in Fig. 6(b). Checkerboard-type modulations of electronic properties around APBs, reflecting the electronic states coupled to the (π, π) type lattice distortions, demonstrate that STM studies of TB and APB can be used to reveal underlying electronic properties of materials (usually hidden in a homogeneous phase), similar to the way single impurity atoms have been used to reveal superconducting properties in high T_C cuprates. Results for different values of E_F are displayed in Fig. 7. Local DOS modulations, particularly the checkerboard type modulations, tend to reach farther into the domain than the elastic texture itself. We also note that the checkerboard type modulations with a wave vector (π, π) are present at any E_F , in contrast to Friedel oscillations for TBs which change wavevectors with E_F .

Although the orbital states and type of electron-lattice

coupling in CMR manganites are quite different from the simple model presented here, our results suggest that simple APBs from double-well type potentials, such as Eq.(3), may give rise to electronic heterogeneities, but not undistorted metallic regions with uniform charge densities near APBs. An energy landscape with a local minimum at undistorted state, such as the one considered in Ref. 14, would be more likely to nucleate metallic domains at APBs, and create percolating conducting paths in CMR manganites.

In summary, we have shown that in functional mate-

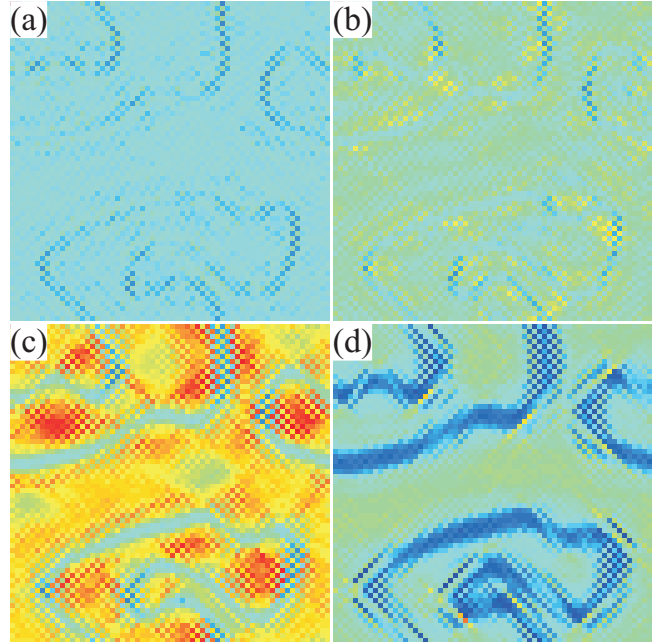


FIG. 7: (Color) Local DOS calculated for the lattice distortion in Fig. 4(b) at various E_F values (a) -1.5, (b) -1.1, (c) -0.7, and (d) -0.3. (dark red: 0.35, dark blue: 0)

rials with strong electron lattice coupling, the electronic properties are modified near elastic textures such as TBs and APBs, which can be directly measured by STM. The results also show that the heterogeneities of electron local DOS are not just confined within TBs and APBs, but can propagate into domains in the form of Friedel oscillations for TBs and with the wave vector of short wave length lattice distortions for APBs.

This work was supported by the US DOE.

* Present address: Advanced Photon Source, Argonne National Laboratory, Argonne, Illinois 60439.

Electronic address: kenahn@aps.anl.gov

¹ M. Uehara *et al.*, Nature **399**, 560 (1999); Ch. Renner *et al.*, *ibid.* **416**, 518 (2002); M. F  th *et al.*, Science **285**, 1540 (1999); L. Zhang *et al.*, *ibid.* **298**, 805 (2002).

² N. Fukumoto *et al.*, Phys. Rev. B **60**, 12963 (1999).

³ A. M. Abakumov *et al.*, Phase Transition **71**, 143 (2000).

⁴ W. Cao, A. Saxena, and D. M. Hatch, Phys. Rev B **64**, 024106 (2001); W. Cao and G. R. Barsch, *ibid.* **41**, 4334 (1990).

⁵ X. Ren and K. Otsuka, MRS Bulletin **27**, 115 (2002).

⁶ Y.-A. Soh *et al.*, Phys. Rev. B **63**, 020402 (2000); Y.-A. Soh *et al.*, J. Appl. Phys. **91**, 7742 (2002).

⁷ See, e.g., J. R. Barkley and W. Jeitschko, J. Appl. Phys. **44**, 938 (1973); V. A. Meleshina *et al.* Sov. Phys. Crys-

- tallogr. **18**, 764 (1974); I. Rychetsky and W. Schranz, J. Phys.: Condens. Matter **5**, 1455 (1993).
- ⁸ K. H. Ahn *et al.*, Phys. Rev. B **68**, 092101 (2003).
- ⁹ G. R. Barsch and J. A. Krumhansl, Phys. Rev. Lett. **53**, 1069 (1984).
- ¹⁰ S. R. Shenoy *et al.*, Phys. Rev. B **60**, R12 537 (1999); T. Lookman *et al.*, *ibid.* **67**, 024114 (2003).
- ¹¹ In 3D, the long-rang interaction due to strain $\sim R^{-3}$.
- ¹² Chap. 28 in S.-k. Ma, *Statistical Mechanics* (World Scientific Publishing Co., Philadelphia, 1985).
- ¹³ S. H. Pan *et al.*, Nature **413**, 282 (2001).
- ¹⁴ K. H. Ahn, T. Lookman, and A. R. Bishop, Nature **428**, 401 (2004).